
MULTIMODAL FUSION FOR FINE-GRAINED CLASSIFICATION OF BREAST FIBROADENOMA AND PHYLLODES TUMORS

Chuxi Nan^{1,2}, Di Wu², Hongming Guo², Ning Cao¹, Xiaohui Zhu^{1,2,3,*}, Zhaoting Shi^{4,5,*}, and Jiawei Li^{4,5,*}

¹School of Integrated Circuits, Wuxi Vocational College of Science and Technology

²School of Advanced Technology, Xi'an Jiaotong-Liverpool University

³Shanghai Gem Science and Technology Co., Ltd.

⁴Department of Oncology, Shanghai Medical College, Fudan University

⁵Department of Medical Ultrasound, Fudan University Shanghai Cancer Center

*Corresponding authors: Xiaohui Zhu, Zhaoting Shi, and Jiawei Li.

June 2026

ABSTRACT

Breast fibroadenoma (FA) and phyllodes tumor (PT) are fibroepithelial breast lesions with highly overlapping appearances on B-mode ultrasound, making benign and borderline PT prone to being misclassified as FA and complicating preoperative decision-making. Existing computer-aided diagnosis methods commonly rely on single-modal imaging features and insufficiently exploit complementary clinical and textual information. To address this limitation, we construct the FAPT-M Dataset, a pathology-confirmed multimodal dataset comprising 910 patients with strictly reviewed ultrasound images, structured clinical attributes, and ultrasound diagnostic descriptions. Based on this dataset, we propose a clinically guided multimodal framework that integrates DenseNet-based visual encoding, CLIP-inspired text encoding, and lightweight clinical encoding, and further introduces clinical-conditioned adaptive modulation, cross-modal Transformer fusion, and dual-path representation learning to improve feature alignment and multimodal interaction. Under patient-level five-fold cross-validation, the proposed method achieves an accuracy of 77.64%, F1-score of 73.38%, and AUC of 89.74%, outperforming representative CNN-, Transformer-, and vision-language-based baselines. Ablation studies and class-balanced evaluations further confirm the contribution of three-modality fusion and the key architectural components. Overall, this work provides an effective multimodal approach for fine-grained FA-PT classification and establishes a high-quality benchmark for multimodal breast ultrasound analysis. The code is available at [GitHub](#)

Keywords Breast ultrasound · Cross-modal interaction · Multimodal learning · Fibroadenoma · Phyllodes tumor

1 Introduction

Breast fibroadenoma (FA) and phyllodes tumor (PT) are biphasic fibroepithelial tumors with overlapping histological characteristics. FA is the most common benign breast tumor, whereas PTs are rare, accounting for 0.3%–1% of cases [1]. PTs are classified into benign, borderline, and malignant subtypes [9]. Clinically, FA is usually managed conservatively or with simple excision [2], while benign and borderline PTs require wide local excision due to higher recurrence risk [6]. Thus, accurate preoperative differentiation between FA and non-malignant PT is critical for surgical decision-making.

Ultrasound is widely used in breast imaging due to its safety, cost-effectiveness, and high sensitivity in dense breast tissue [11, 12]. However, FA and PT exhibit substantial overlap in shape, margin, and echotexture on B-mode ultrasound [3, 4, 7], leading to diagnostic uncertainty and frequent misclassification of PT as FA [3]. Consequently, biopsy or

⁰This work involved human subjects in its research. Approval of all ethical and experimental procedures and protocols was granted by Fudan University Shanghai Cancer Center, China.

postoperative pathology is often required for definitive diagnosis, limiting the reliability of conventional ultrasound interpretation.

Deep learning has achieved strong performance in breast ultrasound analysis, particularly in benign–malignant classification and lesion detection [4, 20]. However, most studies focus on coarse-grained tasks [19, 22], while FA–PT differentiation remains underexplored. Existing works often treat all PT subtypes as a single class against FA [8], ignoring PT heterogeneity (benign, borderline, malignant). This study instead focuses on fine-grained classification of FA, benign PT, and borderline PT, which is more clinically relevant but challenging due to high imaging similarity [13].

The diagnostic difficulty is further amplified by subtle inter-class differences and ultrasound noise [10], as well as the lack of standardized multimodal datasets for FA and PT [17, 21]. Moreover, clinical diagnosis typically integrates imaging, textual reports, and structured data, whereas most existing methods rely solely on images, limiting performance [18].

To address these challenges, we construct a large-scale multimodal dataset, termed the FAPT-M Dataset, consisting of 910 pathology-confirmed cases with ultrasound images, structured clinical variables, and diagnostic text. All cases undergo strict multi-expert review. This dataset better reflects real-world diagnostic workflows.

Based on this dataset, we propose a multimodal deep-learning framework with bidirectional cross-modal attention and gated modulation, enabling adaptive fusion of image, text, and clinical features. Experimental results demonstrate consistent superiority over strong baselines, with robust performance across ablation studies and multi-center validation, indicating strong generalization ability.

The main contributions are summarized as follows:

- We construct a large-scale, pathology-confirmed multimodal dataset for fine-grained classification of FA, benign PT, and borderline PT.
- We propose a multimodal deep learning framework integrating ultrasound images, clinical variables, and diagnostic text for FA–PT differentiation.
- Extensive experiments, including multi-center validation and ablation studies, demonstrate the superiority and robustness of the proposed method in fine-grained lesion classification.

2 Related Work

2.1 Ultrasound-based Breast Tumor Diagnosis

Breast ultrasound (BUS) is widely used for tumor screening and diagnosis due to its radiation-free, cost-effective, and reproducible nature, particularly in dense breast tissue [15]. However, fibroadenoma (FA) and phyllodes tumor (PT) exhibit significant overlap in B-mode ultrasound features, making visual differentiation challenging [5, 7, 9].

Recent deep learning approaches have improved BUS-based analysis, but most focus on benign–malignant classification, general lesion detection, or coarse-grained categorization rather than FA–PT subtype discrimination [14, 53, 54]. Existing FA–PT studies typically simplify the task as binary classification by merging all PT subtypes into one category [8, 16, 21]. In contrast, this work addresses fine-grained three-class classification of FA, benign PT, and borderline PT using multimodal data. To the best of our knowledge, no large-scale pathology-confirmed multimodal dataset has been specifically designed for this task.

2.2 Multimodal in Medical Imaging

Multimodal learning has been widely explored to integrate complementary information from heterogeneous medical data sources. Surveys by Li et al. and Cui et al. demonstrate that multimodal fusion of imaging and non-imaging data (e.g., clinical and pathological information) generally improves diagnostic performance and robustness over unimodal methods [23][24].

Attention-based fusion methods have been proposed to enhance cross-modal interaction and feature aggregation [25]. In breast imaging, integrating ultrasound with mammography improves classification accuracy and AUC compared with single-modality models [18], while multi-view ultrasound fusion further enhances performance in challenging cases [26]. Additionally, combining multiple ultrasound representations such as B-mode and parametric imaging has shown further improvements over single-modality inputs [27].

Table 1: Demographics and clinical characteristics of patients.

Characteristics	FA	B	BD
Number	410	211	255
Ages(Years)	40.15 \pm 12.47	40.13 \pm 11.05	43.70 \pm 11.84
Max diameter(mm)	18.50 \pm 8.14	27.84 \pm 10.68	33.97 \pm 12.07
BI-RADS Categories:			
3	63	47	49
4A	330	134	164
4B	16	27	37
4C	1	3	5

Note: FA = fibroadenoma; B = benign phyllodes tumor; BD = borderline phyllodes tumor; BI-RADS = Breast Imaging Reporting and Data System. BI-RADS categories indicate standardized breast imaging assessment levels, with higher categories generally reflecting greater suspicion of malignancy or the need for further clinical management [55].

2.3 CNN-Based Medical Image Analysis and DenseNet Architectures

CNNs are widely adopted in medical image analysis due to their strong capability in modeling local texture and structural features. Salehi et al. reported that CNNs and transfer learning remain dominant approaches in classification, detection, and segmentation tasks [28]. Sistaninejad et al. further confirmed their effectiveness in feature extraction and discriminative representation learning [29].

Among CNN architectures, DenseNet introduces dense connectivity to improve feature reuse and gradient flow, achieving strong representational power with parameter efficiency [31]. Zhou et al. highlighted its effectiveness in medical image analysis tasks including classification, segmentation, and detection [30]. In breast imaging, DenseNet has demonstrated competitive performance in ultrasound classification [32], mammography analysis [33], and histopathological image recognition [34].

3 Data Annotation and Preprocessing

Although there exist certain similarities between FA and PT in ultrasound images, there remain subtle yet valuable structural disparities among different pathological subtypes, such as internal echo distribution, interstitial structural characteristics, and edge continuity[35][36][37]. These disparities typically change gradually and do not form a distinct category boundary[39][40]. Consequently, higher demands are placed on the accuracy and consistency of data annotation.

In the actual clinical setting, breast sonographers typically do not analyze a single image in isolation. Instead, they conduct a comprehensive assessment by integrating structured clinical data, including the patient’s age, tumour size and growth trend, and standardized diagnostic descriptions[38]. This information can provide supplementary clues about tumour biology and is useful for differentiating fibroepithelial lesions[41][42]. Consequently, when constructing training data for fine-grained classification, it is challenging to fully reflect the actual diagnosis and treatment decision-making process solely by retaining image data.

In this study, during the data construction phase, the pathological results are rigorously adopted as the gold standard. The categories of all cases are verified, and a one-to-one correspondence between images and pathology is established to avoid label noise interfering with model training. During data labeling, multiple experienced breast sonographers conduct cross-reviews to improve classification consistency and reliability. Simultaneously, structured clinical variables (including age, tumor size, and standardized diagnostic text) are systematically integrated, and standardization is completed in the preprocessing stage to offer standardized input for subsequent multimodal feature fusion.

3.1 Data Collection and Ultrasound Image Acquisition

3.1.1 Data Collection

This single-center retrospective study was approved by Fudan University Shanghai Cancer Center, and informed consent was waived. All data were anonymized prior to analysis. A total of 910 patients diagnosed between 2015 and 2025 were included, consisting of 411 FA, 211 benign PTs, and 255 borderline PTs. Patient demographics are summarized in Table 1. The cohort age ranged from 14 to 88 years (median: 41.16 years). Inclusion criteria were: (1) tumor size between 4 mm and 70 mm; (2) surgical resection with postoperative pathological confirmation; and (3) clearly defined

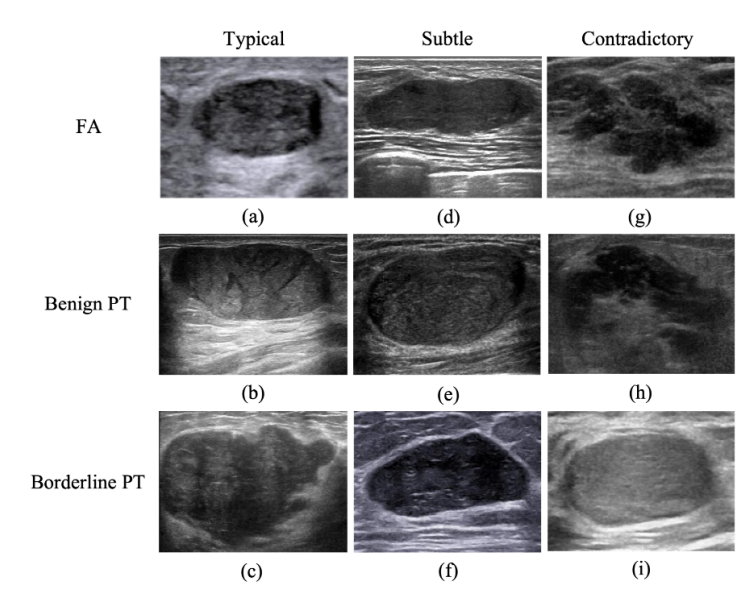


Figure 1: Representative B-mode ultrasound images of FA and PT. (a) FA with regular shape and homogeneous echotexture. (b) Benign PT with relatively circumscribed margin and heterogeneous echotexture. (c) Borderline PT with lobulated margin and heterogeneity. (d)–(f) cases with subtle differences but different pathology. (g)–(i) atypical presentations increasing diagnostic difficulty.

pathological subtypes, particularly distinguishing benign and borderline PTs. These criteria ensure reliable histological ground truth for model training.

3.1.2 Ultrasound Image Acquisition

Ultrasound images were collected using multiple clinical devices, including Philips EPIQ7 and iU22, GE LOGIQ E9, V730, and LOGIQ S8, Mindray Resona 7, and Toshiba Aplio 500. Linear array transducers with 5–12 MHz frequency were used. Panoramic or trapezoidal imaging modes were applied for large lesions to preserve complete structural information.

3.2 Data Annotation and Preprocessing

3.2.1 Data Annotation

Representative ultrasound cases are shown in Fig. 1. Final labels were determined based on postoperative pathology as the gold standard. Pathological slides were independently reviewed by two experienced pathologists (>10 years), with a third senior physician resolving disagreements. Ultrasound lesion annotations were verified by multiple sonographers (8–20 years of experience) using majority voting. Structured clinical data (age, tumor dimensions, ultrasound reports, and diagnostic impressions) were extracted from electronic medical records and cross-validated by two physicians.

3.2.2 Data Preprocessing

All images were originally stored in DICOM format and converted to JPG while preserving grayscale information. ROI cropping was performed based on sonographer-confirmed lesion boundaries, with review by a breast imaging specialist to ensure complete tumor coverage and removal of irrelevant regions such as background tissue and annotations. Finally, images were resized to 224×224 and normalized to $[0,1]$ to reduce inter-device variability and improve training stability.

4 Method

We conduct fine-grained classification of FAs and PTs by jointly modeling ultrasound images, diagnostic text descriptions, and structured clinical variables. This section introduces the proposed clinically guided multimodal fusion

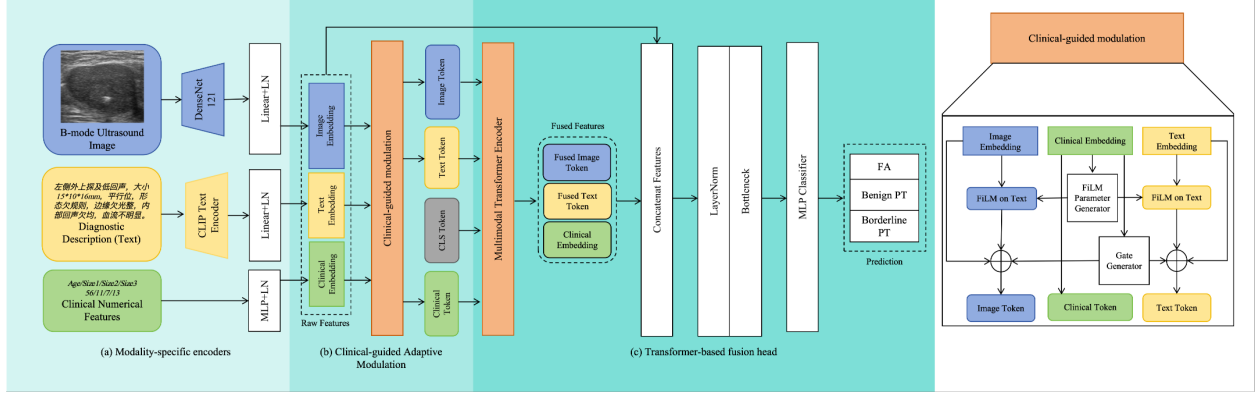


Figure 2: Overview of the proposed method. (a) Modality-specific encoders extract image, text, and clinical embeddings. (b) The Clinical-guided Adaptive Modulation module generates FiLM parameters and adaptive gates from the clinical embedding to modulate the image and text features. (c) A Transformer-based fusion head jointly models modality tokens and combines raw and fused features for final classification.

network, including modality-specific feature encoding, clinically-guided adaptive modulation, and Transformer-based cross-modal fusion and classification, as shown in Fig. 2.

4.1 Modality-Specific Feature Encoding

As shown in Fig. 2(a), the multimodal feature encoding module is designed to extract discriminative high-level semantic representations from heterogeneous information sources and map different modalities into a unified embedding space, thereby providing a stable representation foundation for subsequent conditional modulation and cross-modal interaction modeling. Unlike natural image classification tasks, breast ultrasound diagnosis involves three substantially different modalities: visual images, diagnostic text descriptions, and structured clinical variables. These modalities exhibit significant discrepancies in data distribution, feature structure, and semantic hierarchy. Therefore, direct fusion in their original feature spaces may result in scale inconsistency, distribution shift, and semantic conflicts. To address these challenges, we construct independent encoders for each modality and align them into a shared latent space through a unified projection mechanism.

Let $x \in \mathbb{R}^{H \times W \times 3}$ denote the input ultrasound image, where H and W represent the image height and width, respectively, and the channel dimension of 3 is used to match the input requirement of the ImageNet-pretrained DenseNet121 visual backbone. Let t denote the corresponding ultrasound diagnostic description, and let $c \in \mathbb{R}^{d_c}$ denote the structured clinical feature vector, where d_c represents the number of clinical variables. In the visual branch, the image encoder $E_{\text{img}}(\cdot)$ is implemented using DenseNet121 to extract high-level visual representations from the ultrasound image. The extracted features are expected to capture lesion-related characteristics, including morphology, boundary sharpness, internal echo distribution, and spatial texture patterns. Through hierarchical convolutional operations and nonlinear transformations, the image encoder integrates local structural cues into discriminative visual representations for subsequent multimodal fusion.

In the textual branch, a pretrained language encoder $E_{\text{txt}}(\cdot)$ is utilized to obtain contextualized semantic embeddings, enabling effective encoding of professional terminology and semantic relations within diagnostic descriptions. These representations not only summarize imaging findings but also implicitly capture diagnostic reasoning patterns and expert knowledge, thus providing semantic complementarity to visual features.

In the clinical branch, a multilayer perceptron $E_{\text{clin}}(\cdot)$ is adopted to perform nonlinear mapping of structured variables, modeling latent relationships among diagnostic priors such as patient age and tumor size.

To achieve cross-modal semantic alignment and reduce distribution discrepancies, modality-specific features are projected into a unified embedding space via learnable linear transformations followed by layer normalization:

$$\mathbf{z}_m = \text{LN}(W_m E_m(\cdot)), \quad m \in \{\text{img}, \text{txt}, \text{clin}\}. \quad (1)$$

Here, W_m represents the projection matrix for modality m . This projection unifies feature dimensionality and adjusts modality-dependent statistical distributions, enabling comparability within a shared semantic space. Layer normalization

further reduces discrepancies in scale and variance across modalities, thereby enhancing the stability of subsequent conditional modulation and attention mechanisms.

Finally, \mathbf{z}_{img} , \mathbf{z}_{txt} , and \mathbf{z}_{clin} reside in the same d -dimensional embedding space. This unified representation space can be regarded as a modality-aligned semantic manifold, where heterogeneous information is mapped to consistent feature scales and structural representations. From a learning perspective, this stage achieves the transformation from heterogeneous feature domains to a unified latent space, serving as a prerequisite for clinically conditioned reparameterization and global cross-modal dependency modeling.

4.2 Clinical-Guided Adaptive Modulation

As illustrated in Fig. 1(b), after modality-specific embeddings are obtained, the proposed framework further incorporates structured clinical priors into the feature transformation process through a Clinical-guided Adaptive Modulation module. Although multimodal encoders can extract visual and textual semantic representations independently, they typically assume that different modalities are mutually independent during representation learning, with structured clinical variables merely participating as parallel inputs in the final classification stage. Such a design overlooks the intrinsic *conditional dependency* that characterizes clinical diagnosis. In real-world clinical scenarios, radiologists interpret imaging findings in conjunction with patient-specific information, such as patient age and tumor size, as well as structured diagnostic descriptions derived from ultrasound assessment. Therefore, introducing clinical variables through simple feature concatenation is insufficient to capture the dynamic regulatory effect of clinical priors on the feature representation space. To address this limitation, we propose a clinical-conditioned representation modulation mechanism that directly incorporates structured clinical embeddings into the feature transformation process, explicitly modeling the conditional dependency between clinical variables and modality responses at the representation level.

Let the modality representations in the unified embedding space be $\mathbf{z}_{\text{img}}, \mathbf{z}_{\text{txt}}, \mathbf{z}_{\text{clin}} \in \mathbb{R}^d$. We first utilize the clinical embedding to generate feature-wise modulation parameters:

$$(\boldsymbol{\gamma}, \boldsymbol{\beta}) = f_{\text{film}}(\mathbf{z}_{\text{clin}}), \quad (2)$$

where $\boldsymbol{\gamma}, \boldsymbol{\beta} \in \mathbb{R}^d$ represent channel-wise scaling and shifting coefficients, respectively. This process can be interpreted as a *conditional affine transformation*, whose essence is the dynamic reparameterization of modality representations. Unlike static feature transformations, the modulation parameters are not fixed; instead, they are generated under the guidance of clinical priors, enabling the representation space to deform across different diagnostic contexts adaptively. Specifically, $\boldsymbol{\gamma}$ controls the importance weighting of semantic channels while $\boldsymbol{\beta}$ adjusts feature distribution offsets, enabling channel-wise adaptive reweighting of visual and textual embeddings. This mechanism allows the model to selectively amplify features that are highly relevant to the current clinical context while suppressing potentially irrelevant information.

However, directly applying conditional affine transformations may overly disrupt the original semantic structure, particularly in limited medical data settings where aggressive feature transformations can destabilize representations and induce gradient oscillations. To enhance training stability and regulate modulation strength, we further introduce a gated residual structure. The final modulated representation is defined as:

$$\mathbf{z}^{\text{mod}} = \mathbf{z} + g(\mathbf{z}_{\text{clin}}) \cdot (\boldsymbol{\gamma} \odot \mathbf{z} + \boldsymbol{\beta}), \quad (3)$$

where $g(\cdot)$ represents a learnable gating function constrained within $(0, 1)$ and \odot denotes element-wise multiplication. This structure can be construed as a clinically controlled residual reweighting mechanism: when clinical information provides strong guidance for the current sample, the gating factor increases, enhancing modulation; when the contribution of clinical variables is limited, the model preserves more of the original modality semantics, preventing excessive reliance on structured priors. By maintaining modality-specific semantic stability while introducing condition-driven adaptive feature redistribution, the proposed mechanism enhances the representation space’s sensitivity to subtle differences among fine-grained tumor subtypes.

The modulation process is independently applied to visual and textual embeddings, resulting in $\mathbf{z}_{\text{img}}^{\text{mod}}$ and $\mathbf{z}_{\text{txt}}^{\text{mod}}$. By embedding structured clinical priors into feature-level transformations rather than simple concatenation, the proposed approach explicitly models the conditional dependency structure between clinical variables and modality responses from a representation-learning perspective, enabling dynamic adjustment of feature emphasis across different diagnostic contexts and thereby enhancing discriminative capability and generalization performance.

4.3 Transformer-Based Fusion Head

As shown in Fig. 1(c), after clinical-conditioned modulation, modality representations acquire context-aware semantic structures. However, explicit global dependency modeling across modalities is still lacking. Simple feature concatenation cannot capture the complex interactions among visual, textual, and clinical representations, nor does it achieve fine-grained semantic alignment. To address this limitation, we introduce a transformer-based fusion head that first constructs token-level cross-modal interactions in a unified embedding space and then performs final dual-path fusion for classification.

Let the modulated visual and textual embeddings be denoted as $\mathbf{z}_{\text{img}}^{\text{mod}}$ and $\mathbf{z}_{\text{txt}}^{\text{mod}}$, respectively, and let the clinical embedding be \mathbf{z}_{clin} . We initially treat these three modality representations as independent semantic tokens and construct a multimodal token sequence:

$$\mathbf{T} = [\mathbf{z}_{\text{img}}^{\text{mod}}, \mathbf{z}_{\text{txt}}^{\text{mod}}, \mathbf{z}_{\text{clin}}]. \quad (4)$$

This tokenization strategy maps heterogeneous features into homogeneous representational units, enabling different modalities to interact within a shared attention space. In contrast to fusion strategies based on weighted summation or direct concatenation, token-level representation introduces an additional modeling dimension corresponding to modality identity. This design enables each modality-specific representation to selectively attend to others, thus learning adaptive inter-modality correlations beyond feature-level aggregation.

The token sequence is subsequently fed into a multi-layer transformer encoder, where multi-head self-attention performs global dependency modeling. The self-attention mechanism computes correlation weights among tokens. It dynamically redistributes cross-modal information, allowing visual representations to be refined according to textual semantics and clinical context, and vice versa. Compared with explicitly designed cross-attention structures, the unified self-attention framework avoids imposing artificial hierarchical relationships among modalities. Maintaining symmetry and modality equality during interaction enhances representational stability and prevents biased information flow.

After multiple layers of interaction, the fused modality representations are obtained as

$$\mathbf{T}^{\text{fused}} = [\mathbf{z}_{\text{img}}^f, \mathbf{z}_{\text{txt}}^f, \mathbf{z}_{\text{clin}}^f]. \quad (5)$$

where $\mathbf{z}_{\text{img}}^f$, $\mathbf{z}_{\text{txt}}^f$, and $\mathbf{z}_{\text{clin}}^f$ jointly encode modality-specific semantics and cross-modal contextual dependencies. This interaction mechanism can be interpreted as a global contextual reconstruction process on a unified semantic manifold, where the representation space evolves from condition-aware unimodal embeddings to context-enhanced multimodal representations. By explicitly modeling long-range inter-modality dependencies, the proposed module improves semantic alignment accuracy, reduces information fragmentation, and enhances discriminative capacity and generalization performance in complex fine-grained classification tasks.

After cross-modal interaction modeling, the fused representations encode global contextual dependencies. However, relying solely on interaction-enhanced features for classification may lead to over-smoothing of original modality-specific semantics. While self-attention effectively aggregates cross-modal information, it inevitably redistributes feature weights, potentially attenuating high-frequency discriminative cues. In fine-grained medical classification tasks, subtle yet critical visual patterns or textual indicators may be weakened during global aggregation. To address this issue, we further adopt a dual-path fusion strategy within the fusion head, which simultaneously preserves original modality embeddings and interaction-enhanced representations, thus achieving complementary information integration and representation fidelity.

Specifically, modality-specific embeddings \mathbf{z}_{img} , \mathbf{z}_{txt} , and \mathbf{z}_{clin} constitute the *raw semantic pathway*, retaining local discriminative cues extracted during unimodal encoding. This pathway emphasizes structural integrity and semantic stability. Meanwhile, transformer-refined embeddings $\mathbf{z}_{\text{img}}^f$, $\mathbf{z}_{\text{txt}}^f$, and $\mathbf{z}_{\text{clin}}^f$ form the *cross-modal pathway*, capturing contextual dependencies and semantic alignment across modalities. The two pathways are integrated through concatenation to form a comprehensive fusion representation:

$$\mathbf{z}_{\text{fusion}} = \text{Concat}(\mathbf{z}_{\text{img}}, \mathbf{z}_{\text{txt}}, \mathbf{z}_{\text{clin}}, \mathbf{z}_{\text{img}}^f, \mathbf{z}_{\text{txt}}^f, \mathbf{z}_{\text{clin}}^f). \quad (6)$$

This design can be interpreted as an explicit complementary information mechanism: the raw pathway preserves modality-specific discriminative capacity. In contrast, the interaction pathway introduces global semantic coherence and cross-modal synergy. Compared with using only fused features or only raw embeddings, the dual-path structure

establishes a balance between representational stability and expressive power. It ensures that critical local information is retained while benefiting from contextual enhancement provided by cross-modal interaction.

Subsequently, the fused representation is normalized and transformed through a nonlinear classification head to obtain the final prediction:

$$\hat{y} = \text{Classifier}(\mathbf{z}_{\text{fusion}}). \quad (7)$$

The classification head consists of fully connected layers with nonlinear activation and regularization, constructing the final decision boundary within the fused representation space. By jointly leveraging original semantic features and interaction-enhanced representations, the proposed dual-path fusion mechanism forms a residual-style semantic compensation structure at the representation level. This design enhances robustness and generalization while maintaining expressive richness, making it particularly suitable for fine-grained tumor subtype classification tasks that are highly sensitive to subtle local variations.

5 Experiments

5.1 Implementation Details

All experiments were conducted using patient-level splitting to avoid data leakage, ensuring that images from the same patient do not appear in both training and validation sets. For main experiments, patients were partitioned into five folds based on patient ID. In each round of cross-validation, four folds were used for training and one for validation, ensuring each patient appears in the validation set exactly once. All baseline methods followed the same partitioning strategy to ensure fair comparison.

For ablation studies, the same patient-level split was used. Unless otherwise specified, experiments were conducted on the first fold to reduce computational cost while maintaining consistency in data separation. Structured clinical variables, including age and tumor size measurements, were normalized using z-score standardization based on training set statistics, and the same parameters were applied to validation and test sets to avoid leakage. Diagnostic text was processed separately by the text encoder.

All models were trained for 100 epochs with a learning rate of 1×10^{-4} and batch size of 32 using cross-entropy loss. Experiments were conducted on an NVIDIA RTX 4090 GPU (24 GB), with Python 3.12, PyTorch 2.5.1, CUDA 12.4, running on Ubuntu 22.04. The system was equipped with a 16-core Intel Xeon Platinum 8358P CPU and 120 GB RAM.

5.2 Evaluation Metrics

We report accuracy (ACC), precision, recall, F1-score, sensitivity, specificity, area under the curve (AUC), and negative log-likelihood (NLL). Due to class imbalance, all metrics are computed using macro-averaging. Specifically, precision, recall, and F1-score are calculated per class and averaged. Sensitivity and specificity are computed using a one-vs-rest strategy. AUC is also evaluated under the one-vs-rest scheme. NLL is computed as the average negative log-probability of the true class and used to assess calibration performance. Accuracy is reported as an overall performance indicator. Results are reported as mean \pm standard deviation. Best results are highlighted in bold. Statistical significance is assessed using a paired t-test, with *, **, and *** indicating $p < 0.05$, 0.01, and 0.001, respectively.

5.3 Comparative Experiments

To evaluate the effectiveness of the proposed multimodal framework, we conduct systematic comparative experiments against several representative convolutional neural network (CNN) and Transformer-based architectures under a unified experimental protocol. For fairness, all models are trained and evaluated using identical data preprocessing procedures, optimization strategies, and evaluation criteria.

As reported in Table 2, the proposed method achieves the best overall performance across most evaluation metrics. In terms of ACC and F1-Score, the proposed model consistently outperforms representative CNN and Transformer baselines such as DenseNet[31], EfficientNetV2[43], Swin[44], and DeiT[47]. These results indicate that the proposed multimodal fusion strategy can effectively enhance classification performance.

In terms of PRE and REC, the proposed method also achieves the highest scores among the comparison models. Similarly, the Sensitivity and Specificity indicate that the model maintains balanced performance across different categories. In addition, the proposed framework achieves the highest AUC, demonstrating stronger discrimination

Table 2: Comparative Experiment Results on the FAPT-M Dataset

Method	ACC(%)	F1-Score(%)	PRE(%)	REC(%)	Sensitivity(%)	Specificity(%)	AUC	NLL
Swin	73.93±2.2*	66.97±3.9	68.12±1.7	66.76±4.0	66.76±4.0	85.89±3.2	84.11±2.8*	0.81±0.8
ResNet	71.37±4.4**	64.19±2.2**	65.16±3.0	63.56±1.3	63.56±1.3	84.33±4.4	82.05±0.9**	0.82±0.7
DenseNet	74.64±1.1	68.62±3.7	69.08±2.6	68.58±3.8	68.58±3.8	86.66±1.1	86.81±4.2	1.01±1.0
EfficientNetV2	73.65±3.2	68.38±0.8	69.49±4.5	69.06±2.8	69.06±2.8	86.42±2.1	88.06±3.3	1.60±1.4
ViT	64.67±1.8***	55.12±4.8***	59.39±2.5	55.25±1.8	55.25±1.8	79.74±3.8	78.13±4.2***	0.81±0.9
DeiT	73.36±4.2	67.71±1.8	67.42±3.9	68.14±0.8	68.14±0.8	86.46±1.1	87.17±2.5	1.30±1.2
CLIP	66.10±3.7**	59.75±2.5	60.78±4.3	60.24±1.6	60.24±1.6	81.61±0.7	76.81±3.4**	1.05±1.0
Ours	77.64±1.7	73.38±3.2	73.08±0.9	73.77±2.2	73.77±2.2	88.56±4.1	89.74±3.9	1.28±0.7

Table 3: Class-wise Comparison and Ablation Experiment Results on the Balanced FAPT-M Subset

Category	ResNet(%)	DenseNet(%)	EfficientNetV2(%)	Swin(%)	DeiT(%)	Image(%)	Image+Clinical(%)	Image+Text(%)	Ours(%)
FA	75.00±4.5	87.50±2.2	72.50±1.7	85.00±3.5	80.00±4.0	85.00±2.5	87.50±1.2	85.00±3.5	92.50±0.8
B	42.50±3.8	47.50±4.5	52.50±2.2	65.00±1.3	40.00±3.9	55.00±3.0	67.50±4.4	50.00±2.8	60.00±1.7
BD	72.50±2.7	70.00±1.8	45.00±3.8	52.50±4.2	80.00±0.4	60.00±2.7	55.00±3.0	80.00±1.2	70.00±2.9
Total	63.33±1.9	68.33±2.4	56.67±3.9	67.50±0.5	66.67±1.8	66.67±2.8	70.00±3.0	71.67±4.1	74.17±3.8

Table 4: Binary FA–PT Classification Comparison and Ablation Experiment Results on the FAPT-M Dataset

Category	ResNet(%)	DenseNet(%)	EfficientNetV2(%)	Swin(%)	DeiT(%)	Image Only(%)	Image+Clinical(%)	Image+Text(%)	Ours(%)
FA	82.15±3.1	85.30±4.7	85.36±2.7	85.04±1.8	83.73±3.0	84.51±4.9	81.99±2.1	89.76±1.2	88.45±2.4
PT	82.87±2.0	87.54±1.5	82.15±3.1	87.54±2.5	87.23±0.6	89.35±1.3	93.46±3.8	86.92±2.7	90.97±1.1
Total	82.48±4.0	86.32±2.6	83.62±1.9	86.18±3.6	85.33±2.8	86.75±1.5	87.18±4.5	88.46±3.4	89.60±2.2

Table 5: Module-Level Ablation Experiment Results on the Balanced FAPT-M Subset

Method	ACC(%)	F1-Score(%)	PRE(%)	REC(%)	Sensitivity(%)	Specificity(%)	AUC	NLL
Only-Fused	73.79±1.2	69.27±3.8	68.66±2.5	70.40±4.1	70.40±4.1	87.37±0.9	88.27±3.2	1.36±2.8
w/o Bottleneck	75.50±2.7	70.69±1.5	70.60±4.3	70.84±0.8	70.84±0.8	87.17±3.5	89.00±2.1	1.19±1.4
w/o CLS Token	76.64±4.0	72.90±2.9	72.20±1.7	74.09±3.3	74.09±3.3	88.69±2.2	89.32±0.7	1.29±4.2
w/o Gate	75.78±3.1	70.70±4.5	70.47±2.3	71.13±1.9	71.13±1.9	87.75±0.6	89.38±3.8	1.56±2.5
w/o FiLM	75.21±0.8	71.47±3.2	70.79±4.0	72.93±2.6	72.93±2.6	87.97±1.8	89.76±3.0	1.30±1.1
Ours	78.06±2.4	72.63±1.3	73.55±3.7	72.57±0.9	72.57±0.9	88.43±4.1	89.77±2.8	1.57±3.5

capability across different decision thresholds. Statistical analysis further confirms that the performance improvements are significant compared with most baseline methods.

To further investigate whether the performance improvement is influenced by class distribution, we construct a class-balanced subset containing 200 samples for each subcategory (FA, B, and BD). As shown in Table 3, the proposed method still achieves the best overall ACC under this controlled setting. At the class level, the model performs particularly well for FA and maintains competitive performance for the other subcategories. These results indicate that the proposed framework maintains its advantage even after class imbalance is eliminated.

Furthermore, to simulate a clinically simplified diagnostic scenario and prove the generalization of the proposed method, we conduct additional binary classification experiments by merging benign and borderline PT into a single PT category. The results are summarized in Table 4. The proposed model achieves the best overall performance and maintains consistent improvements across both FA and PT categories.

Overall, the experimental results demonstrate that the proposed multimodal framework achieves superior performance in fine-grained breast tumor classification compared with conventional CNNs, Transformers, and modality-limited models.

Table 6: Modality Contribution Ablation Experiment Results on the Balanced FAPT-M Subset

Method	ACC(%)	F1-Score(%)	PRE(%)	REC(%)	Sensitivity(%)	Specificity(%)	AUC	NLL
Image Only	73.65±4.5	68.39±1.9	67.94±3.1	69.18±2.8	69.18±2.8	87.35±0.8	86.94±4.2	1.39±1.2
Image+Clinical	74.50±3.1	69.51±4.0	69.01±2.0	70.25±1.6	70.25±1.6	87.55±3.0	88.82±1.3	0.94±0.9
Image+Text	76.78±0.8	72.56±2.4	72.35±3.5	73.16±4.3	73.16±4.3	88.10±1.9	90.31±2.1	1.14±1.0
Ours	77.64±1.7	73.38±3.2	73.08±0.9	73.77±2.2	73.77±2.2	88.56±4.1	89.74±3.9	1.28±0.7

5.4 Ablation Studies

5.4.1 Module-Level ablation

To further validate the necessity of each key component within the proposed multimodal framework, we conduct systematic ablation experiments to evaluate the contributions of the dual-path fusion strategy, structural modules, and the clinical-conditioned modulation mechanism. All ablation variants are trained and evaluated under the same data partition and experimental settings to ensure a fair comparison. The quantitative results of the module-level ablation study are summarized in Table 5.

To examine the dual-path fusion strategy, we construct a Solely-Fused variant that retains only the Transformer interaction-enhanced representations while removing the original modality-specific path. As shown in Table 5, this variant yields lower performance than the complete model, indicating that relying solely on interaction-enhanced features may weaken modality-specific discriminative information. We further investigate the impact of structural components by removing the bottleneck layer and the Classification (CLS) token. Compared with the full model, removing the Bottleneck leads to performance degradation, suggesting that the bottleneck helps stabilize the high-dimensional fused representation. For the variant without the CLS Token, although F1-Score, REC, and Sensitivity are slightly improved, its ACC and AUC decrease compared with the full model. This suggests that the CLS token mainly contributes to global cross-modal aggregation and overall discriminative ability, rather than improving all metrics uniformly.

In addition, we evaluate the clinical-conditioned modulation mechanism by removing the Gate module and further removing the FiLM module. Both ablations result in consistent performance drops, indicating that clinical-guided modulation plays an important role in adaptive feature adjustment across modalities. Overall, Table 5 shows that the complete model achieves the best overall performance among all ablation variants, and removing any key component results in reduced performance across multiple metrics, demonstrating that these modules collectively contribute to the effectiveness and stability of the proposed framework.

5.4.2 Modality Contribution

To further evaluate the contribution of different input modalities (ultrasound images, ultrasound diagnostic descriptions, and structured clinical variables) to the overall performance, we conduct modality ablation experiments by constructing four variants. All models adopt the same backbone and training strategy, differing only in the modality combination of input data to ensure a fair comparison.

In the modality contribution ablation study, the Only Image Modality model was taken as the baseline. Incorporating structured clinical variables into the baseline model leads to a noticeable improvement in performance, indicating that structured clinical information can provide supplementary diagnostic clues that complement the visual information from ultrasound images. A more significant performance enhancement is observed when ultrasound diagnostic descriptions are added to the image input, demonstrating that the textual information in these descriptions effectively enriches the model’s understanding of the clinical context and improves its discriminative ability.

Finally, the proposal model (Ours) that integrates all three modalities achieves optimal overall performance, outperforming all single- and dual-modal variants. This model also shows enhanced performance in terms of sensitivity and specificity, reflecting its stronger ability to correctly identify positive cases and accurately exclude negative cases, as detailed in Table 6.

Overall, the results in Table 6 consistently demonstrate that the integration of clinical variables and ultrasound diagnostic descriptions can improve model performance compared to the image-only baseline. The full multimodal configuration, which combines all three input modalities, delivers the most robust and comprehensive results across various evaluation metrics, confirming the value of fusing multi-source clinical information for the task at hand.

Table 7: Modality Contribution Ablation Study on Balanced Subset (General Metrics, 200 Samples per Subcategory)

Method	ACC(%)	F1-Score(%)	PRE(%)	REC(%)	Sensitivity(%)	Specificity(%)	AUC	NLL
Image Only	66.67±2.1	66.41±3.8	66.53±1.9	66.67±2.1	66.67±2.1	83.33±4.2	82.02±3.5	1.08±0.9
Image+Clinical	70.00±1.5	69.58±2.9	69.43±4.1	70.00±1.5	70.00±1.5	85.00±2.5	84.71±0.8	0.69±1.2
Image+Text	71.67±4.3	71.30±1.7	72.56±2.5	71.67±4.3	71.67±4.3	85.83±3.4	82.10±4.0	1.01±0.7
Ours	74.17±0.9	73.90±4.5	74.42±3.2	74.17±0.9	74.17±0.9	87.08±1.3	87.31±2.9	1.67±1.5

Table 8: Module-Level Ablation Study on Balanced Subset (General Metrics, 200 Samples per Subcategory)

Method	ACC(%)	F1-Score(%)	PRE(%)	REC(%)	Sensitivity(%)	Specificity(%)	AUC	NLL
Only-Fused	70.83±3.6	70.34±1.2	70.11±4.4	70.83±3.6	70.83±3.6	85.42±0.5	86.85±2.0	1.37±1.3
w/o Bottleneck	70.83±2.6	71.47±4.0	73.04±1.5	70.83±2.6	70.83±2.6	85.42±3.5	83.78±0.9	0.75±0.8
w/o CLS Token	71.67±1.3	71.94±3.8	72.71±2.6	71.67±1.3	71.67±1.3	85.83±4.3	85.96±3.1	1.27±1.2
w/o Gate	72.50±4.2	72.21±0.7	72.18±3.7	72.50±4.2	72.50±4.2	86.25±2.3	86.07±1.0	0.69±1.4
w/o FiLM	71.67±0.8	71.33±2.8	71.12±1.1	71.67±0.8	71.67±0.8	85.83±3.4	84.60±2.3	0.73±0.9
Ours	74.17±0.9	73.90±4.5	74.42±3.2	74.17±0.9	74.17±0.9	87.08±1.3	87.31±2.9	1.67±1.5

Table 9: Ablation Study on Balanced Subset (Class-wise ACC, 200 Samples per Subcategory)

Method	FA(%)	B(%)	BD(%)
Image Only	85.00±4.5	55.00±3.2	60.00±1.7
Image+Clinical	87.50±3.9	67.50±4.4	55.00±2.8
Image+Text	85.00±2.3	50.00±1.9	80.00±3.1
Only-Fused	92.50±4.5	67.50±2.7	52.50±3.0
w/o Bottleneck	87.50±1.2	62.50±4.8	72.50±2.4
w/o CLS Token	87.50±2.9	60.00±1.8	67.50±0.7
w/o Gate	90.00±3.8	65.00±2.8	62.50±4.1
w/o FiLM	87.50±4.2	72.50±1.4	55.00±3.9
Ours	92.50±4.0	60.00±2.6	70.00±3.8

5.5 Class-Balanced Analysis

To provide a more in-depth analysis of the influence of class distribution on model performance, we construct a class-balanced subset for additional comparative experiments. Specifically, an equal number of samples is randomly selected for each tumor subtype (FA, B, and BD) to form a balanced class subset. Under this setting, we retrain and evaluate the unimodal, bimodal, and full multimodal models to reduce the potential confounding effect introduced by class imbalance.

The results of the balanced-subset experiments are reported in Table 7, and the corresponding subtype-wise accuracies are shown in Table 9. From the overall performance perspective, the proposed model (Ours) achieves competitive performance under the balanced setting, although it does not obtain the best value for every individual metric. Compared with the image-only modality baseline, incorporating additional modalities generally improves the overall discriminative ability, and the complete multimodal configuration provides a balanced trade-off among different evaluation metrics. This indicates that the proposed multimodal framework can retain stable performance even when class distribution is controlled.

From the subtype-wise perspective, the proposed model (Ours) achieves the highest accuracy on FA and maintains competitive accuracy on B and BD. The Image+Text variant achieves the highest accuracy on BD, indicating that ultrasound diagnostic descriptions contribute to performance on this subtype. In contrast, the image-only baseline performs relatively poorly on B, suggesting that ultrasound images alone are insufficient for distinguishing this subtype in a balanced setting.

We further evaluate module-level ablation variants on the balanced subset. Removing key components, including the bottleneck layer, CLS token, Gate, or FiLM module, results in lower overall ACC than the complete model, indicating that these components remain beneficial even when the class distribution is balanced.

Overall, within the class-balanced setting, the complete multimodal model retains advantages in both overall and subtype-wise performance. These results suggest that the observed performance improvements are not solely due to class distribution bias, and the proposed framework maintains consistent discriminative capability across different tumor subtypes under controlled class proportions.

6 Discussion

6.1 Comparison With State-of-the-Art Methods

The proposed multimodal framework achieves competitive performance compared with CNN-based, Transformer-based, and vision-language models. CNNs are effective in capturing local texture patterns and morphological details but are limited in modeling long-range dependencies. Transformers model global context effectively but may underutilize fine-grained spatial priors in ultrasound images. Vision-language models such as CLIP provide strong semantic representations but require task-specific adaptation for fine-grained medical classification.

In contrast, the proposed method integrates ultrasound images, diagnostic text, and structured clinical variables within a unified framework. The clinical-conditioned modulation and cross-modal interaction modules enable adaptive feature fusion while preserving modality-specific information. Experimental results demonstrate consistent superiority over strong baselines, indicating the benefit of explicitly modeling multimodal complementarity for fine-grained breast tumor classification.

From a clinical perspective, FA, benign PT, and borderline PT exhibit highly overlapping ultrasound appearances. Incorporating textual and clinical information provides complementary diagnostic cues, reducing reliance on image-only patterns and improving robustness in ambiguous cases.

6.2 Contribution of Multimodal Information

Different modalities provide complementary information for tumor classification. Ultrasound images capture morphological and echo characteristics, diagnostic text encodes radiological interpretations, and structured clinical variables provide patient-specific context. Their combination enhances discriminative representation, especially when imaging features are highly similar across subtypes.

The results suggest that multimodal fusion improves robustness by incorporating semantic and clinical cues beyond visual appearance. This aligns with clinical practice, where diagnosis is based on integrated imaging, reporting, and patient information rather than images alone.

6.3 Effect of Clinical-Conditioned Modulation and Cross-Modal Interaction

The ablation study shows that performance gains are not only due to multimodal inputs but also the fusion strategy. Direct concatenation is insufficient to capture complex cross-modal relationships. In contrast, clinical-conditioned modulation and Transformer-based interaction enable adaptive feature recalibration and cross-modal dependency modeling.

The FiLM-based modulation uses clinical variables to guide feature emphasis, while the gating mechanism controls modality contributions to reduce redundancy. The Transformer fusion module further enables global interaction among modality tokens. The bottleneck layer improves compactness and reduces overfitting, and the CLS token provides global aggregation for multimodal representation learning. Overall, the full model achieves a better balance between accuracy and robustness.

6.4 Class-Balanced and Class-wise Performance Analysis

Class-balanced evaluation indicates that the proposed model maintains strong performance independent of class distribution. FA is generally easier to distinguish, whereas benign and borderline PT show higher overlap, making subtype discrimination more challenging even under balanced settings.

Multimodal fusion helps mitigate this issue by incorporating complementary information beyond imaging appearance. Clinical and textual cues provide additional discriminative signals, improving robustness in ambiguous cases and ensuring more stable class-wise performance.

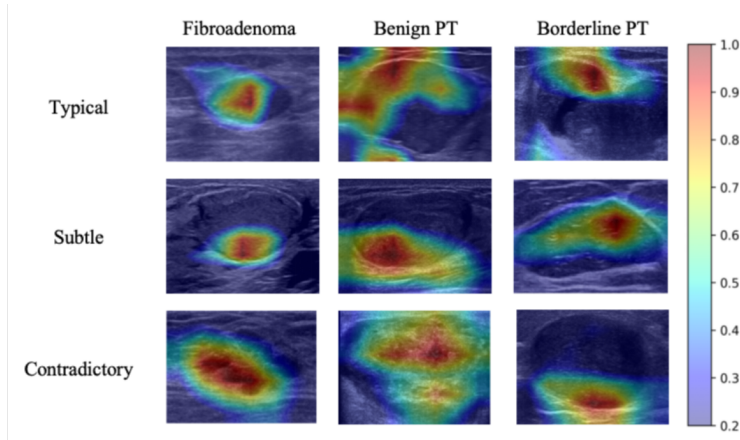


Figure 3: Representative Grad-CAM images of breast fibroadenoma (FA) and phyllodes tumor (PT). Red regions indicate areas that contribute more strongly to the model prediction, while blue regions indicate regions with lower contribution.

6.5 Interpretability Analysis via Grad-CAM

Grad-CAM visualizations show that the model focuses primarily on lesion regions rather than background tissue. In typical cases, attention is concentrated on clinically relevant structures such as lesion boundaries and internal echo patterns. In subtle or challenging cases, the model still attends to intra-lesional regions, indicating its ability to capture fine-grained discriminative cues. In atypical cases, attention remains localized within tumor regions, suggesting robustness against irrelevant background interference.

These results support the interpretability of the proposed framework and enhance its potential clinical trustworthiness.

6.6 Generalization Ability Analysis

The model maintains stable performance across different experimental settings, including class-balanced and simplified classification tasks, indicating robust multimodal representation learning. The complementary nature of multiple modalities reduces dependence on any single feature type, improving stability under varying data conditions. However, the current study is based on a single-center retrospective dataset. External validation on multi-center cohorts is required to further evaluate generalization performance.

6.7 Limitations and Future Work

This study has several limitations. First, the dataset is single-center and class-imbalanced, which may affect representation stability despite class-balanced experiments. Multi-center datasets with improved distribution balance are needed for further validation. Second, the current framework focuses on image-level classification and does not incorporate explicit lesion segmentation. Integrating segmentation or localization may further enhance feature learning. Finally, only B-mode ultrasound, diagnostic text, and structured clinical variables are used. Additional imaging modalities such as elastography, Doppler, and contrast-enhanced ultrasound may further improve performance in future work.

7 Conclusion

In this paper, we proposed a multimodal deep learning framework for fine-grained classification of FA and PT tumors using ultrasound data, ultrasound diagnostic text, and clinical variables. By integrating ultrasound images, diagnostic text descriptions, and structured clinical information, the model leverages complementary information from multiple modalities to better capture subtle differences between highly similar lesions. The proposed bidirectional cross-modal attention and gated modulation mechanisms enable effective semantic alignment and adaptive feature fusion across modalities. Experimental results demonstrate that the proposed method consistently outperforms several strong baseline models and maintains stable performance across ablation studies and multi-center validation, indicating robustness and generalization. These findings suggest that multimodal learning can improve diagnostic accuracy in challenging breast tumor differentiation tasks. Future work will focus on expanding the dataset scale, incorporating additional clinical modalities, and further validating the framework in prospective clinical settings.

References

- [1] M. D. Rowell, R. R. Perry, J. G. Hsiu, and S. C. Barranco, "Phyllodes tumors," *Am J Surg*, vol. 165, no. 3, pp. 376–379, Mar. 1993, doi: 10.1016/s0002-9610(05)80849-9. PMID: 8383473.
- [2] R. Greenberg, Y. Skornick, and O. Kaplan, "Management of breast fibroadenomas," *J Gen Intern Med*, vol. 13, no. 9, pp. 640–645, Sep. 1998, doi: 10.1046/j.1525-1497.1998.cr188.x. PMID: 9754521; PMCID: PMC1497021.
- [3] H. Tan et al., "Imaging findings in phyllodes tumors of the breast," *Eur J Radiol*, vol. 81, no. 1, pp. e62–e69, Jan. 2012, doi: 10.1016/j.ejrad.2011.01.085. Epub 2011 Feb 25; PMID: 21353414.
- [4] S. P. Mishra, S. K. Tiwary, M. Mishra, and A. K. Khanna, "Phyllodes tumor of breast: a review article," *ISRN Surg*, vol. 2013, p. 361469, 2013, doi: 10.1155/2013/361469.
- [5] C. Wiratkapun, P. Piyapan, P. Lertsithichai, and N. Larbcharoensub, "Fibroadenoma versus phyllodes tumor: distinguishing factors in patients diagnosed with fibroepithelial lesions after a core needle biopsy," *Diagn Interv Radiol*, vol. 20, no. 1, pp. 27–33, Jan. 2014, doi: 10.5152/dir.2013.13133. PMID: 24356293; PMCID: PMC4463252.
- [6] T. Adesoye, H. B. Neuman, L. G. Wilke, J. R. Schumacher, J. Steiman, and C. C. Greenberg, "Current Trends in the Management of Phyllodes Tumors of the Breast," *Ann Surg Oncol*, vol. 23, no. 10, pp. 3199–3205, Oct. 2016, doi: 10.1245/s10434-016-5314-0. Epub 2016 Jun 22; PMID: 27334214; PMCID: PMC5021443.
- [7] L. Duman, N. S. Gezer, P. Balcı, C. Altay, I. Başara, M. G. Durak, and A. I. Sevinç, "Differentiation between Phyllodes Tumors and Fibroadenomas Based on Mammographic Sonographic and MRI Features," *Breast care*, vol. 11, no. 2, pp. 123–127, 2016, doi: 10.1159/000444377.
- [8] E. Stoffel et al., "Distinction between phyllodes tumor and fibroadenoma in breast ultrasound using deep learning image analysis," *Eur J Radiol Open*, vol. 5, pp. 165–170, Sep. 2018, doi: 10.1016/j.ejro.2018.09.002.
- [9] M. Kalambo et al., "Phyllodes Tumor of the Breast: Ultrasound-Pathology Correlation," *AJR Am J Roentgenol*, vol. 210, no. 4, pp. W173–W179, Apr. 2018, doi: 10.2214/AJR.17.18554. Epub 2018 Feb 7; PMID: 29412020.
- [10] S. Liu, Y. Wang, X. Yang, B. Lei, L. Liu, S. X. Li, D. Ni, and T. Wang, "Deep Learning in Medical Ultrasound Analysis: A Review," *Engineering*, vol. 5, no. 2, pp. 261–275, 2019, ISSN: 2095-8099, doi: 10.1016/j.eng.2018.11.020. URL: <https://www.sciencedirect.com/science/article/pii/S2095809918301887>.
- [11] V. Suvannarerg, P. Chitchumngong, W. Apiwat et al., "Diagnostic performance of qualitative and quantitative shear wave elastography in differentiating malignant from benign breast masses, and association with the histological prognostic factors," *Quant Imaging Med Surg*, vol. 9, no. 3, pp. 386–398, 2019, doi: 10.21037/qims.2019.03.04.
- [12] F. Pediconi and F. Galati, "Breast cancer screening programs: does one risk fit all?," *Quant Imaging Med Surg*, vol. 10, no. 4, pp. 886–890, 2020, doi: 10.21037/qims.2020.03.14.
- [13] S. Niu et al., "Differential diagnosis between small breast phyllodes tumors and fibroadenomas using artificial intelligence and ultrasound data," *Quant Imaging Med Surg*, vol. 11, no. 5, pp. 2052–2061, 2021, doi: 10.21037/qims-20-919.
- [14] R. Wilding, V. M. Sheraton, L. Soto, N. Chotai, and E. Y. Tan, "Deep learning applied to breast imaging classification and segmentation with human expert intervention," *J Ultrasound*, vol. 25, no. 3, pp. 659–666, Sep. 2022, doi: 10.1007/s40477-021-00642-3. PMID: 35000127; PMCID: PMC9402837.
- [15] R. Iacob et al., "Evaluating the role of breast ultrasound in early detection of breast cancer in low- and middle-income countries: a comprehensive narrative review," *Bioengineering*, vol. 11, no. 3, p. 262, Mar. 2024, doi: 10.3390/bioengineering11030262.
- [16] Y. Yan et al., "Deep learning-assisted distinguishing breast phyllodes tumours from fibroadenomas based on ultrasound images: a diagnostic study," *Br J Radiol*, vol. 97, no. 1163, pp. 1816–1825, 2024, doi: 10.1093/bjr/tqae147.
- [17] F. F. Abir, A. E. Daly, K. Anderman, T. Ozmen, and L. J. Brattain, "Multimodal Deep Learning for Phyllodes Tumor Classification from Ultrasound and Clinical Data," in *2025 IEEE 21st Int. Conf. Body Sensor Networks (BSN)*, 2025, pp. 1–4. URL: <https://api.semanticscholar.org/CorpusID:281080211>.
- [18] J. Chen, T. Pan, Z. Zhu et al., "A deep learning-based multimodal medical imaging model for breast cancer screening," *Sci Rep*, vol. 15, p. 14696, 2025, doi: 10.1038/s41598-025-99535-2.
- [19] W. Hu et al., "Performance of artificial intelligence-assisted ultrasound elastography in classifying benign and malignant breast tumors: a systematic review and meta-analysis," *BMC Med Imaging*, vol. 25, no. 1, p. 440, Nov. 2025, doi: 10.1186/s12880-025-01982-w.
- [20] H. Liu et al., "Deep Learning Based on Automated Breast Volume Scanner Images for the Diagnosis of Breast Lesions: A Multicenter Diagnostic Study," *Int J Med Sci*, vol. 22, no. 15, pp. 3924–3937, 2025, doi: 10.7150/ijms.118430.

- [21] G. Lu et al., “Intra-tumor and peritumoral radiomics and deep learning based on ultrasound for differentiating fibroadenoma and phyllodes tumor: a multicenter study,” *Front Oncol*, vol. 15, p. 1668793, Oct. 2025, doi: 10.3389/fonc.2025.1668793.
- [22] A. Mashekova et al., “Review of Artificial Intelligence Techniques for Breast Cancer Detection with Different Modalities: Mammography, Ultrasound, and Thermography Images,” *Bioengineering*, vol. 12, no. 10, p. 1110, Oct. 2025, doi: 10.3390/bioengineering12101110.
- [23] Y. Li et al., “A review of deep learning-based information fusion techniques for multimodal medical image classification,” *Comput. Biol. Med.*, vol. 177, p. 108635, 2024, doi: 10.1016/j.compbiomed.2024.108635.
- [24] C. Cui et al., “Deep multimodal fusion of image and non-image data in disease diagnosis and prognosis: a review,” *Prog. Biomed. Eng.*, vol. 5, no. 2, 2023, doi: 10.1088/2516-1091/acc2fe.
- [25] M. Albekairi et al., “Multimodal medical image fusion combining saliency perception and generative adversarial network,” *Sci. Rep.*, vol. 15, no. 1, p. 10609, Mar. 2025, doi: 10.1038/s41598-025-95147-y.
- [26] T. R. Wei, A. Chang, Y. Kang, M. Patel, Y. Fang, and Y. Yan, “Multimodal deep learning for enhanced breast cancer diagnosis on sonography,” *Comput. Biol. Med.*, vol. 194, p. 110466, Aug. 2025, doi: 10.1016/j.compbiomed.2025.110466.
- [27] S. Muhtadi and C. M. Gallippi, “Breast tumor diagnosis via multimodal deep learning using ultrasound B-mode and Nakagami images,” *J. Med. Imaging*, vol. 12, no. Suppl 2, p. S22009, Nov. 2025, doi: 10.1117/1.JMI.12.S2.S22009.
- [28] A. W. Salehi et al., “A study of CNN and transfer learning in medical imaging: advantages, challenges, future scope,” *Sustainability*, vol. 15, no. 7, p. 5930, 2023, doi: 10.3390/su15075930.
- [29] B. Sistaninejhad, H. Rasi, and P. Nayeri, “A review paper about deep learning for medical image analysis,” *Comput. Math. Methods Med.*, vol. 2023, p. 7091301, May 2023, doi: 10.1155/2023/7091301.
- [30] T. Zhou, X. Ye, H. Lu, X. Zheng, S. Qiu, and Y. Liu, “Dense convolutional network and its application in medical image analysis,” *Biomed. Res. Int.*, vol. 2022, p. 2384830, Apr. 2022, doi: 10.1155/2022/2384830.
- [31] G. Huang, Z. Liu, L. Van Der Maaten, and K. Q. Weinberger, “Densely connected convolutional networks,” in 2017 IEEE Conference on Computer Vision and Pattern Recognition (CVPR), Honolulu, HI, USA, 2017, pp. 2261–2269, doi: 10.1109/CVPR.2017.243.
- [32] A. AlZoubi et al., “Classification of breast lesions in ultrasound images using deep convolutional neural networks: transfer learning versus automatic architecture design,” *Med. Biol. Eng. Comput.*, vol. 62, no. 1, pp. 135–149, 2024, doi: 10.1007/s11517-023-02922-y.
- [33] T. Liao et al., “Classification of asymmetry in mammography via the DenseNet convolutional neural network,” *Eur. J. Radiol. Open*, vol. 11, p. 100502, Jul. 2023, doi: 10.1016/j.ejro.2023.100502.
- [34] X. Li et al., “Classification of breast cancer histopathological images using interleaved DenseNet with SENet (IDSNet),” *PLoS One*, vol. 15, no. 5, p. e0232127, May 2020, doi: 10.1371/journal.pone.0232127.
- [35] T. Kamitani et al., “Differentiation between benign phyllodes tumors and fibroadenomas of the breast on MR imaging,” *Eur. J. Radiol.*, vol. 83, no. 8, pp. 1344–1349, 2014, doi: 10.1016/j.ejrad.2014.04.031.
- [36] W. Lohitvisate et al., “Clinical presentation and radiologic imaging findings of phyllodes tumors: benign and borderline/malignant phyllodes tumors,” *F1000Research*, vol. 13, p. 210, May 28, 2024, doi: 10.12688/f1000research.145872.2.
- [37] L. Duman, L. et al., “Differentiation between phyllodes tumors and fibroadenomas based on mammographic, sonographic and MRI features,” *Breast Care*, vol. 11, no. 2, pp. 123–127, 2016, doi: 10.1159/000444377.
- [38] L. Wu, “Value of High Frequency Ultrasound Parameters in Differential Diagnosis of Breast Phyllodes Tumor and Breast Fibroadenoma,” *Journal of Kunming Medical University*, vol. 33, no. 10, 2012.
- [39] G. Krings, G. R. Bean, and Y. Y. Chen, “Fibroepithelial lesions; The WHO spectrum,” *Semin. Diagn. Pathol.*, vol. 34, no. 5, pp. 438–452, Sep. 2017, doi: 10.1053/j.semmdp.2017.05.006.
- [40] E. A. Rakha et al., “Classification of fibroepithelial lesions of the breast in core needle biopsy with implications for further management,” *Mod. Pathol.*, vol. 38, no. 5, p. 100734, 2025, doi: 10.1016/j.modpat.2025.100734.
- [41] Y. N. Reis et al., “Core needle biopsy in fibroepithelial tumors: predicting factors for phyllodes tumors,” *Clinics (Sao Paulo)*, vol. 76, p. e2806, Apr. 16, 2021, doi: 10.6061/clinics/2021/e2806.
- [42] C. Wiratkapun et al., “Fibroadenoma versus phyllodes tumor: distinguishing factors in patients diagnosed with fibroepithelial lesions after a core needle biopsy,” *Diagn. Interv. Radiol.*, vol. 20, no. 1, pp. 27–33, 2014, doi: 10.5152/dir.2013.13133.

- [43] M. Tan and Q. V. Le, “EfficientNet: Rethinking model scaling for convolutional neural networks,” in *Proc. Int. Conf. Mach. Learn. (ICML)*, 2019, pp. 6105–6114.
- [44] Z. Liu et al., “Swin transformer: Hierarchical vision transformer using shifted windows,” in 2021 IEEE/CVF International Conference on Computer Vision (ICCV), 2021, pp. 9992–10002, doi: 10.1109/ICCV48922.2021.00986.
- [45] A. Radford et al., “Learning transferable visual models from natural language supervision,” 2021, arXiv:2103.00020 [cs.CV].
- [46] A. Dosovitskiy et al., “An image is worth 16x16 words: Transformers for image recognition at scale,” 2021, arXiv:2010.11929 [cs.CV].
- [47] H. Touvron et al., “Training data-efficient image transformers & distillation through attention,” 2021, arXiv:2012.12877 [cs.CV].
- [48] C. C. Atabansi et al., “A survey of Transformer applications for histopathological image analysis: New developments and future directions,” *Biomed. Eng. Online*, vol. 22, no. 1, p. 96, Sep. 2023, doi: 10.1186/s12938-023-01157-0.
- [49] C. C. Atabansi, J. Nie, H. Liu, Q. Song, L. Yan, and X. Zhou, “A survey of Transformer applications for histopathological image analysis: New developments and future directions,” *Biomed. Eng. Online*, vol. 22, no. 1, p. 96, Sep. 2023, doi: 10.1186/s12938-023-01157-0.
- [50] J. W. Kim, A. U. Khan, and I. Banerjee, “Systematic review of hybrid vision transformer architectures for radiological image analysis,” *J. Imaging Inform. Med.*, vol. 38, no. 5, pp. 3248–3262, Oct. 2025, doi: 10.1007/s10278-024-01322-4.
- [51] J. Shreffler and M. R. Huecker, *Diagnostic Testing Accuracy: Sensitivity, Specificity, Predictive Values and Likelihood Ratios*. StatPearls Publishing, 2023.
- [52] R. R. Selvaraju, M. Cogswell, A. Das, R. Vedantam, D. Parikh and D. Batra, Grad-CAM: Visual Explanations from Deep Networks via Gradient-Based Localization. IEEE, 2017.
- [53] M. Alotaibi, B. Alotaibi, A. Razaque and O. Alotaibi, Breast cancer classification based on convolutional neural networks: A systematic review. PeerJ Computer Science, 2023.
- [54] Q. Dan, Z. Xu, H. Burrows, J. Bissram, J. S. A. Stringer and Y. Li, Diagnostic performance of deep learning in ultrasound diagnosis of breast cancer: A systematic review. npj Precision Oncology, 2024.
- [55] American College of Radiology, ACR BI-RADS Atlas: Breast Imaging Reporting and Data System. Reston, VA, USA: American College of Radiology, 2013.